UC Davis

UC Davis Previously Published Works

Title

Ultrafine microporous and mesoporous activated carbon fibers from alkali lignin

Permalink

https://escholarship.org/uc/item/0cv9v4fn

Journal

Journal of Materials Chemistry A, 1(37)

ISSN

2050-7488

Authors

Hu, Sixiao

Hsieh, You-Lo

Publication Date

2013

DOI

10.1039/c3ta12538f

Peer reviewed

eScholarship.org Powered by the California Digital Library
University of California

Journal of Materials Chemistry A

RSC Publishing

PAPER

Ultrafine microporous and mesoporous activated carbon fibers from alkali lignin

Cite this: *J. Mater. Chem. A*, 2013, **1**, 11279

Sixiao Hu and You-Lo Hsieh*

A facile and sustainable approach has been successfully devised to fabricate ultrafine (100–500 nm) highly porous activated carbon fibers (ACFs) by electrospinning of aqueous solutions of predominantly alkali lignin (low sulfonate content) followed by simultaneous carbonization and activation at 850 °C under N_2. Incorporating a polyethylene oxide (PEO) carrier with only up to one ninth of lignin not only enabled efficient electrospinning into fibers but also retained fibrous structures during heating, alleviating the need for a separate thermal stabilization step. *In situ* impregnation of alkali hydroxide activating chemicals with only up to 50% of the lignin carbon precursor, *i.e.*, merely one tenth to one quarter of the quantities used in manufacturing activated carbon particulates, allowed simultaneous carbonization and activation in a single heating step. A range of micropore-dominant to mesopore-dominant ACFs were successfully fabricated to achieve superior specific surface (>1400 $m^2\ g^{-1}$) and porosity (>0.7 $cm^3\ g^{-1}$) tuned by varying the type and contents of alkali hydroxides. This streamlined approach was robust and demonstrated the feasibility and versatility in processing and converting a readily available renewable carbon precursor, lignin, into highly porous activated carbon fibers.

Received 29th June 2013
Accepted 9th July 2013

DOI: 10.1039/c3ta12538f

www.rsc.org/MaterialsA

1 Introduction

Lignin, the second most abundant biopolymer in nature, is a major by-product of chemical pulping and has become increasingly available in high quantity from biofuel production. In spite of chemical heterogeneity as well as source- and process-dependent structural variations, lignin's high carbon content and phenolic structure make it an excellent alternative carbon source and a substitute for petroleum-based carbon products. Notably, the desirable high mass retention characteristic of lignin in thermal processing[1] has been commonly recognized in its conversion to carbon fibers (CFs)[2–5] and porous activated carbon (PAC) particles.[6–11] Differently isolated lignins have been mixed with synthetic polymers, *i.e.*, polyethylene oxide (PEO),[2] polypropylene and polyethylene terephthalate,[3] to be melt spun into fibers and then pyrolyzed into the graphitic form of CFs at temperatures exceeding 1000 °C. These lignin-based CFs were micrometers in diameters and had comparable mechanical properties to commercial polyacrylonitrile-based CFs for reinforcing composites. PACs are high specific surface non-graphitic porous powders or granulates in tens of micrometer to millimeter sizes, usually produced at temperatures less than 1000 °C.[12] Lignin-based PAC particles are commonly chemically activated using phosphoric acid,[7] alkali carbonates,[7] alkali hydroxides[9,11,13,14] or zinc chloride,[7,13] with alkali hydroxides being most effective and frequently used. Kraft lignin-based PACs, for instance, were optimally activated by either sodium hydroxide (NaOH) or potassium hydroxide (KOH) to lignin impregnation ratios above 3.[11] Typically, high specific surface (>1000 $m^2\ g^{-1}$) and pore volume (>0.5 $cm^3\ g^{-1}$) PACs require alkali hydroxide/carbon precursor ratios greater than two,[11,15,16] *i.e.*, the significant input of activating chemicals.

Activated carbon fibers (ACFs) are porous carbon fibers and are usually produced *via* activation of CFs. ACFs are superior to PAC in several ways. The fibrous form of ACFs makes them easy to handle and to be fabricated into different forms of textiles, felts and composites that are versatile for applications. With diameters one to three orders of magnitude smaller than PACs, ACFs have significantly higher specific surfaces, shorter diffusive paths and more accessible pores to sorbates to be used in removing toxic gases, such as SO_2,[17] NO_x,[18] volatile organic compounds[19] and natural gas,[20] in water purification,[21,22] and as capacitors[23,24] and vapor sensors.[25] To date, lignin-based ACFs have only been reported on precursor fibers either melt spun from softwood acetic acid lignin[26] or electrospun from Alcell lignin in ethanol.[27] Although these precursor fibers are one order of magnitude different in diameters, *i.e.*, 20–30 μm for melt spun *vs.* 800 nm to 3 μm for electrospun, both ACFs have high BET surfaces and pore volumes (1930 $m^2\ g^{-1}$ and 0.523 $cm^3\ g^{-1}$ *vs.* 1195 $m^2\ g^{-1}$ and 0.520 $cm^3\ g^{-1}$). Both precursor fibers, however, required thermal stabilization at very low heating rates (2 *vs.* 0.05 °C min^{-1}) in the 200 to 250 °C range over extended lengths of time (1 h *vs.* 36 h) prior to carbonization at 1000 °C. In fact, lengthy stabilization and multi-step

Fiber and Polymer Science, University of California, Davis, One Shields Avenue, Davis, California, 95616, USA. E-mail: ylhsieh@ucdavis.edu

This journal is © The Royal Society of Chemistry 2013

heating that are common not only for ACFs but also for CFs and PAC make these thermal processes to carbon products particularly energy consuming.

This study was aimed at developing a more sustainable approach to fabricate ultra-fine ACFs by using the abundantly available and under-utilized lignin as a carbon precursor and processing into carbon with minimal thermal and chemical input. Aqueous processing was made possible by using highly water-soluble alkali lignin with low sulfonate content (AL_{ls}). The thermal behavior and the associated chemical structural changes of crude AL_{ls} were closely examined to minimize time and energy input in carbonization. A water-soluble, fiber-forming PEO carrier was added at minimum levels to aid electrospinning of AL_{ls} into predominantly lignin hybrid fibers. PEO is thermally stable in the 200 to 250 °C region, and thus also helps to retain fiber forms during heating to alleviate the need for a separate and time-consuming thermal stabilization pretreatment. Two alkali hydroxide activating chemicals, *i.e.*, NaOH and KOH, were *in situ* incorporated in the aqueous mixtures and optimized by studying the properties of ACFs at varied reduced quantities. Carbonization without separate stabilization was carried out at up to either 600 or 850 °C and the properties of ACFs were characterized to relate to the alkali hydroxide compositions and heating processes.

2 Experimental

2.1 Chemicals

Poly(ethylene oxide) (PEO) ($M_w = 600$ kDa) and alkali lignin (low sulfonate content) (AL_{ls}) ($M_w = 60$ kDa, spruce origin) were acquired from Sigma-Aldrich (USA), and sodium hydroxide (anhydrous pellets, A.C.S. grade, 85% minimum purity) and potassium hydroxide (anhydrous pellets, A.C.S. grade 97% minimum purity) were acquired from Fisher Scientific (USA). All the chemicals were used as received.

2.2 Synthesis of lignin-based CFs and ACFs

2.2.1 Electrospinning. For CF precursors, aqueous AL_{ls}–PEO mixtures were prepared by dissolving AL_{ls} and PEO in water at three w/w ratios of 7.4/2.6, 8.6/1.4 and 9/1 and total concentrations of 10.8, 11.7 and 10 wt%, respectively. For ACF precursors, alkali hydroxides of NaOH and KOH were *in situ* incorporated in the solution with 9/1 AL_{ls}–PEO mixture at alkali hydroxide/lignin ratios of 0.1, 0.3 and 0.5. Each AL_{ls}–PEO mixture was electrospun according to a previously reported method.[28,29] Briefly, the mixture was loaded into a 20 mL syringe (Popper & Sons, Inc.) with a 24-gauge BD PrecisionGlide needle with an internal diameter of 0.56 mm (BD, USA), fed at a rate of 1 mL h^{-1} with a syringe pump (KDS 200, KD Scientific, USA) and charged at 10 to 15 kV DC power (ES 30-0.1 P, Gamma High Supply, USA). The electrospun fibers were continuously collected for up to 12 h on a copper mesh (25 cm × 25 cm) vertically placed 12 to 20 cm from the tip of the needle. The electrospun fiber mats were detached from the copper mesh by gently peeling with tweezers and stored over desiccants for further processing and characterization.

2.2.2 Carbonization and activation. To convert AL_{ls}–PEO fibers to CFs without impregnating alkali hydroxides, electrospun precursor fiber mats were rolled and placed in a quartz tube (2 cm inner diameter) of an electric furnace (Mini-Mite, Lindberg/Blue). Carbonization was performed by heating at 10 °C min^{-1} to 105 °C and holding for 0.5 h to drive off the moisture, then heating to either 600 or 850 °C and holding for 0.5 h, all under flowing N_2 at 100 mL min^{-1}. The heat processed fibers were cooled to ambient temperature within 12 h, also under flowing N_2 at 100 mL min^{-1}. To prepare spin dopes for ACFs, NaOH and KOH were added at 0.1, 0.3 and 0.5 alkali hydroxide/AL_{ls} weight ratios in the aqueous AL_{ls}–PEO mixtures. Simultaneous carbonization and activation of these electrospun precursor fibers were carried out the same way as for CFs to 850 °C to produce ACFs. Both CFs and ACFs were washed with deionized water to remove residual alkali metals and other small hydrocarbon impurities, and then dried at 105 °C for 0.5 h.

2.3 HCl washing of crude lignin

Sodium in crude AL_{ls} was removed by dissolution with a 5 wt% aqueous HCl solution to examine its effects on lignin's thermal properties. A 10 wt% aqueous AL_{ls} solution (40 g) was prepared by dissolving crude AL_{ls} in H_2O under constant stirring for 6 h, and to which, 200 g of a 5 wt% aqueous HCl solution was added, stirred for 3 h, and then centrifuged (Centrifuge 5804R, Eppendorf) at 4000 rpm for 15 min to obtain filtrate 1 and precipitate 1. Precipitate 1 was added to 200 g of H_2O to form a colloid, stirred for 3 h, then centrifuged (4000 rpm, 15 min) to obtain filtrate 2 and precipitate 2. The same dissolution and centrifugation procedure was repeated with precipitate 2 to obtain precipitate 3 and filtrate 3. When precipitate 3 was dissolved in 200 g of H_2O, a clear solution was formed yielding no precipitate after centrifugation and was referred to as filtrate 4. The filtrates were dried over $CaCl_2$ desiccant under vacuum for 7 days and weighed to 1 mg (BP-300s, Sartorius) to calculate the yields in percentage from each step.

2.4 Analytical methods

The chemical structures of crude, HCl washed AL_{ls} and pyrolyzed AL_{ls} were examined by Fourier transform infrared spectroscopy (FTIR) (Nicolet 6700, Thermo Scientific). Crude AL_{ls} was heated at 10 °C min^{-1} to specific elevated temperatures, from 150 to 500 °C, under a 30 mL min^{-1} N_2 flow in a differential scanning calorimeter (DSC) (DSC-60, Shimadzu). The solid residues were cooled to room temperature within 3 h. All FTIR spectra were collected from the samples dried at 60 °C for 12 h and pressed with anhydrous KBr powder into pellets. The thermal properties of the AL_{ls} and as-electrospun fibers were analyzed by DSC and thermogravimetric analysis (TGA) (TGA-50, Shimadzu). DSC samples, tightly packed in aluminum pans, covered and press-sealed, were heated at 10 °C min^{-1} to 500 °C under a 30 mL min^{-1} N_2 flow. TGA samples were heated at 10 °C min^{-1} to 600 °C under a 50 mL min^{-1} N_2 flow. The atomic compositions of crude, HCl washed AL_{ls} products and ACFs were carried out by energy-dispersive X-ray spectroscopy (EDX)

 This journal is © The Royal Society of Chemistry 2013

adjunct to a scanning electron microscope (SEM) (FEI-XL 30, FEI). Crude AL_{ls} was characterized as received, and HCl washed AL_{ls} products were characterized after drying over desiccants for 2 days while ACFs were washed thoroughly with deionized water and dried at 60 °C for 0.5 h before EDX measurements. The morphologies and structures of the as-electrospun fibers and ACFs were observed using SEM, atomic force microscopy (AFM) (MFP 3D, Asylum Research) and transmission electron microscopy (TEM) (JEOL 3000, JEOL). SEM samples were sputter coated with gold for 1 min and observed under a working voltage of 5 kV. TEM samples were prepared by dispersing a small amount of ACFs in water (~0.01 g L^{-1}), placing a drop of the suspension on a carbon grid, and then letting them dry in air. AFM samples were prepared by dispersing a small amount of ACFs in acetone (~0.01 g L^{-1}), placing a drop of the suspension on a glass slide, and then letting them dry in air. The fibers were analyzed with a silicon tip (AC160 TS, Olympus) in the tapping mode. For surface area and pore characterization, crude AL_{ls} powder, CFs and ACFs were dried at 50 °C for 48 h, and then measured at 77 K using a nitrogen adsorption–desorption analyzer (ASAP 2020, Micromeritics). The single point total pore volume was estimated from the adsorption branch of the isotherm at a relative pressure P/P_o close to 1. The Brunauer–Emmett–Teller (BET) surface area was calculated from the isotherm in the BET linear region where the relative pressure P/P_o ranged from 0.05 to 0.3. The mesopore surface area was derived from the adsorption branch, whereas pore and neck size distributions were derived from both adsorption and desorption branches of the isotherm using the Barrett–Joyner–Halenda (BJH) method. The micropore surface area and pore hydraulic diameter distribution from 0.7 to 1.6 nm were derived from the *t*-plot using the Mikhail, Brunauer and Bodor MP method[30] and the Harkins & Jura equation.[31] Micropore volume (V_{mp}) was derived from the tangent line of a contiguous range of the *t*-plot using the surface area of the filled pores *via* eqn (1),

$$V_{mp} = \frac{(S_n - S_{n-1}) \times (t_n - t_{n-1})}{2} \times 15.47 \quad (1)$$

where S_n and t_n are the surface area derived from the slope of the tangent and the thickness of the absorbed layer at the *n* point in the *t*-plot, respectively, and 15.47 is the constant for converting gas volume to liquid volume at STP.

3 Results and discussion

3.1 AL_{ls} structures and thermal behaviors

The chemical compositions of AL_{ls} and its chemical structural changes from pyrolysis at varying elevated temperatures were characterized by EDS and FTIR, respectively, and correlated to the thermal transitions observed by DSC and TGA to associate chemical changes with thermal transitions. AL_{ls} consisted of 64.1% C, 29.1% O, 4.6% S and 3.2% Na as determined by EDX. The S and Na present in AL_{ls} were thought to be in the form of sodium sulfonate and phenolate, which were reaction products of native lignin and pulping chemicals, such as sodium sulfite, sodium hydroxide and bisulfite salts. Both phenolic and aliphatic hydroxyl (–OH) groups as well as phenylpropanoid structures characteristic of lignin are clearly evident from the FTIR spectrum of AL_{ls}. The –OH related peaks include the hydrogen bonded –OH at 3430 cm^{-1} and free –OH at 2930 and 2835 cm^{-1} as well as C–O deformation in primary aliphatic and secondary ether/aliphatic –OH at 1031 and 1081^{-1} cm, respectively. The phenylpropanoid peaks located mainly in the 1600 to 1000 cm^{-1} region (Fig. 1a), *i.e.*, aromatic skeletal vibrations at 1596 and 1513 cm^{-1}, overlapping of various carbonyl (C=O) groups as extensive peak broadening at 1596 cm^{-1}, aromatic ring stretching with C=O at around 1270 cm^{-1} and aromatic C–H in-plane deformation near 1130 cm^{-1}. The FTIR spectrum of AL_{ls} clearly shows –OH groups and phenylpropanoid structures that are responsible respectively for water solubility and tranforming lignin into polycyclic aromatic/nonaromatic hydrocarbon building-blocks during carbonization, the key underlying structural characteristic of great carbon precursors.[32]

The FTIR spectrum of AL_{ls} pyrolytic residues from different temperatures suggested that little or no chemical changes occurred below 250 °C, with only an endotherm around 90 °C accompanied by a 6% mass loss from the loss of moisture. As the pyrolysis temperature increased to 300 °C, the FTIR showed clear decreased 2930 and 2835 cm^{-1} peaks associated with the free –OH groups that disappeared at 350 °C, possibly from the oxidation of AL_{ls} phenolic structures to quinone methides,

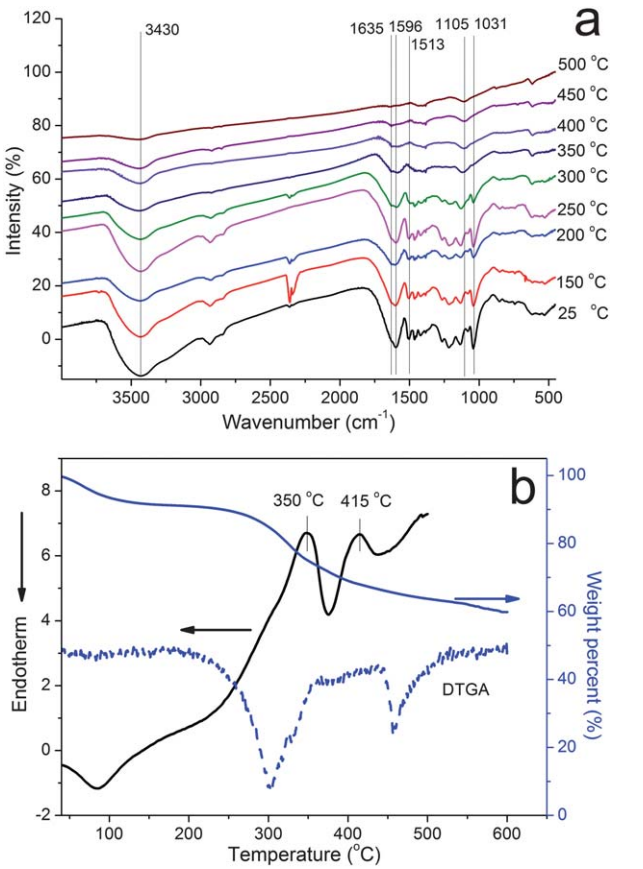

Fig. 1 AL_{ls} characteristics: (a) FTIR spectra of pyrolyzed AL_{ls} at varying temperatures; (b) DSC and TGA thermographs (10 °C min^{-1}, N_2).

the intermediates in pyrolyzing lignin phenols to hydrocarbons.[33] For AL_{ls} pyrolyzed at 400 °C, both C=C stretching at 1635 cm^{-1} and aromatic skeletal stretching at 1596 cm^{-1} decreased significantly. The phenylpropanoid characteristic peaks between 1600 cm^{-1} and 1000 cm^{-1} disappeared, showing the absence of aromatic structures at 450 °C. The shifting aromatic C–H in plane bending from 1130 cm^{-1} to 1105 cm^{-1} also suggests the loss of substituent groups on the aromatic rings. Correspondingly, the largest major exotherm from 250 to 375 °C peaking at 350 °C, and a smaller one between 375 and 435 °C peaking at 415 °C were associated with the most significant 28% mass loss (from 94% to 66%) and another 6% loss. Upon heating to 500 °C, the aromatic skeletal stretching peaks at 1598 and 1513 cm^{-1} disappeared, corresponding to a small exotherm approaching 500 °C and a further 10% mass loss, leaving 60% mass at 600 °C, suggesting further decomposition of lignin quinone methides, elimination of substitute groups and formation of various polycyclic hydrocarbons, consistent with the pyrolysis-gas chromatography-mass spectroscopy of different lignins and lignin sulfonates.[34,35]

The above thermal and chemical characterization results showed AL_{ls} to be thermally stable at up to 225 °C, showing major thermal transformations between 225 °C and 375 °C and most chemical structural changes in the 300 to 400 °C range. The –OH significantly decreased at 300 °C and completely disappeared at 350 °C, implying the oxidation of phenolic hydroxyls to quinone methide structures, followed by the loss of the characteristic phenylpropanoid and its substituents at 400 °C. The chemical changes may include the cleavages of intermolecular linkages into small volatile phenol derivatives reported on alkali lignins from tobacco[34] and hardwood.[36] The 63.7 wt% pyrolyzed solid at 500 °C gave little evidence of the aromatic skeletal structure and exothermic charring continued with further heating, leaving 60% of the product at 600 °C.

3.2 Electrospun AL_{ls}–PEO and PEO fibers

As aqueous solutions at any concentration, AL_{ls} alone could not be electrospun into fibers. Adding the easily electrospinnable PEO carrier to as little as one ninth of AL_{ls} made these aqueous mixtures electrospinnable into fibers. Further reducing PEO to 5% of AL_{ls} could not sustain continuous electrospinning. The aqueous AL_{ls}–PEO mixtures at 7.4/2.6, 8.6/1.4 and 9/1 w/w compositions were successfully electrospun at the rate of 1 mL h^{-1} continuously for up to 12 h, forming thick fibrous membranes that consisted of fine, smooth fibers with diameters ranging from 500 nm to 1.5 μm (Fig. 2). The fibers electrospun from the 9/1 AL_{ls}–PEO mixture were slightly smaller than the others, possibly due to lower solution viscosity. The fiber size distribution at each composition was relatively uniform.

Crude PEO powders melt at 68 °C and exhibited two decomposition exotherms: a small one at 355 °C and another larger one at 420 °C (Fig. 3a). The corresponding TGA thermograph showed PEO to be stable below 250 °C, losing 6.5% mass gradually at up to 355 °C, then a significant 89% mass loss between 355 and 440 °C, leaving only 2.1% residue at 600 °C (Fig. 3b). PEO was clearly more thermally stable in the 225 to 375 °C temperature range where AL_{ls} showed major thermal transformations and chemical structural changes. This confirmed the stabilizing role of PEO, one of the primary functions of PEO in the hybrid fibers. All three as-electrospun AL_{ls}–PEO hybrid fibers showed small moisture evaporation endotherms near 100 °C and broad shallow exotherms spanning between 200 and 450 °C, the latter showing no resemblance to either AL_{ls} or PEO. None exhibited the melting peak of PEO, indicating PEO domains in these AL_{ls}–PEO hybrid fibers to be non-crystalline. This suggested that the 10 to 26% PEO in the

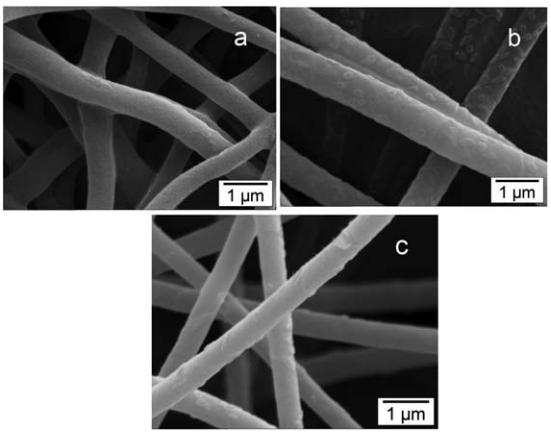

Fig. 2 SEM images of AL_{ls}–PEO hybrid fibers electrospun from aqueous AL_{ls} solutions at: (a) 7.4/2.6; (b) 8.6/1.4; (c) 9/1 (w/w) ratios.

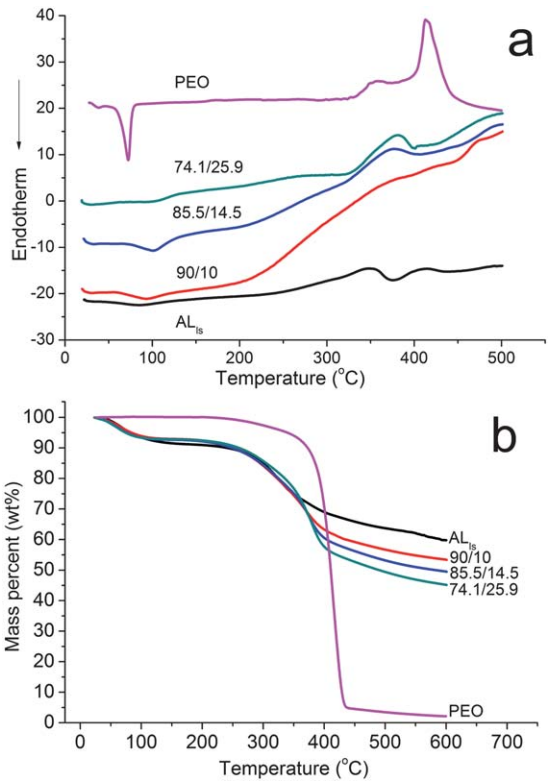

Fig. 3 Thermal properties of electrospun AL_{ls}–PEO hybrid fibers: (a) DSC; (b) TGA thermographs.

This journal is © The Royal Society of Chemistry 2013

hybrid fibers was either not phase separated from AL_{ls}, *i.e.*, fully inter-mixed, or phase separated but in insufficient quantity to crystallize. That AL_{ls}–PEO mixtures could be electrospun indicated that PEO must be well mixed with AL_{ls} while providing chain entanglement to enable fiber formation. Decomposition of PEO in the hybrid fibers also occurred at lower temperatures compared to that in electrospun PEO, possibly due to its non-crystalline structure.

The as-electrospun AL_{ls}–PEO hybrid fibers (Fig. 3b) showed similar mass loss profiles as AL_{ls} and correlated well with their compositions or AL_{ls} contents. Residual mass at 600 °C was 45, 50 and 54 wt% for 7.4/2.6, 8.6/1.4 and 9/1 AL_{ls}–PEO hybrid fibers, respectively, again consistent with their AL_{ls} contents based on the 60% residue of AL_{ls} at 600 °C. This observation suggested pyrolysis of either AL_{ls} or PEO in the AL_{ls}-dominant hybrid fibers to be independent of each other and no chemical interactions between AL_{ls} and PEO during carbonization. These results confirmed that carbonization of AL_{ls} was not affected by the presence of PEO, another promising aspect of these AL_{ls}–PEO combinations.

The DSC and TGA results indicated that PEO was miscible with AL_{ls} to facilitate fiber formation by electrospinning, but not crystallized in the hybrid fibers. Lignin in the AL_{ls}–PEO hybrids, on the other hand, showed independent pyrolysis behavior. The favorable role of PEO was thus confirmed in that it facilitated electrospinning at relatively low contents and provided thermal stability for AL_{ls} from 225 to 375 °C for fiber shape retention, while not interfering with thermal decomposition and structural transformation of lignin to carbon char. These observations also imply that volumes occupied by PEO, whether minimally phase separated or not, may be retained during decomposition and carbonization to create microporosity.

3.3 Carbon fibers (CFs) and activated carbon fibers (ACFs)

NaOH and KOH activating chemicals were *in situ* incorporated in 10 wt% aqueous 9/1 AL_{ls}–PEO mixtures which were electrospun into fibers then pyrolyzed into ACFs. The alkali hydroxides were added to the AL_{ls}–PEO mixtures at the 1/10, 3/10 and 1/2 alkali hydroxide/AL_{ls} ratios. Adding either alkali hydroxides reduced the fiber diameters, *i.e.*, slightly to the 300 to 500 nm range for NaOH and more significantly to the 100 to 300 nm range for KOH (Fig. 4). The decreased fiber sizes are generally attributed to the increased charges of the solutions and/or improved charge dissipation with the added electrolytes in electrospinning. The smaller KOH-containing fibers may be due to the effect of a stronger base.

CFs and ACFs were carbonized by heating (10 °C min^{-1} under N_2) to 600 °C and 850 °C, respectively. CF and ACFs activated with 50 wt% NaOH and KOH showed similarly high carbon contents of 93.4, 94.4 and 93.7 wt%, respectively, with the rest being oxygen by EDX analysis. SEMs of CFs and ACFs showed no dimensional change or inter-fiber fusion (Fig. 4). The absence of inter-fiber fusion is significant and confirms that thermal stabilization pretreatment is unnecessary. This further affirms that PEO is not only miscible with AL_{ls} but also provides the necessary dimensional stability to retain the fibrous shape. The infusibility of CFs could also be attributed to inter- and intra- molecular crosslinking of AL_{ls} below 250 °C, in the earlier stage of carbonization, consistent with the observation made on softwood (*e.g.* spruce) lignin based carbon fibers.[37] For ACFs, infusibility may be further attributed to the presence of alkali hydroxides which have been shown to increase the char yield from lignin.[38] Therefore, the effects of sodium on the properties of AL_{ls} were further investigated.

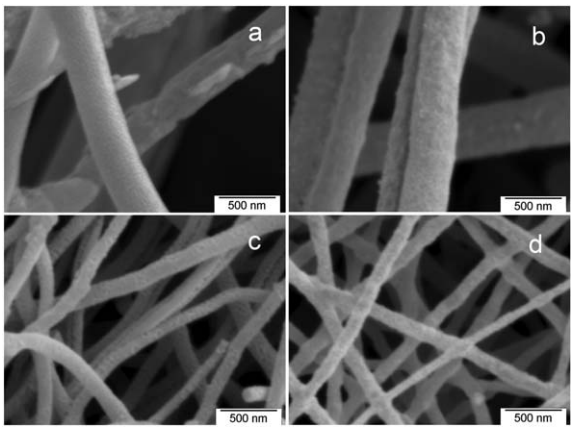

Fig. 4 SEM images of 9/1 AL_{ls}–PEO hybrid fibers with NaOH (a and b) and KOH (c and d) at a 0.5 alkali hydroxide/AL_{ls} ratio: (a and c) as-electrospun; (c and d) carbonized (850 °C, 0.5 h, N_2).

3.4 Effects of sodium on the thermal properties of lignin

Crude AL_{ls} contained 3.2 wt% Na which is expected to affect the thermal transitions and pyrolysis pathways as well as the activation of lignin. To study its role, Na in AL_{ls} was released into the aqueous solution by mixing with 5 wt% aqueous HCl, followed by water rinsing. A portion of Na in AL_{ls} became soluble NaCl when reacting with HCl and remained in filtrate 1 (Fig. 5a), while the precipitates consisted of AL_{ls} with less Na whose contents decreased with further water rinsing until none was found in filtrate 4 (Fig. 5d). The FTIR spectra of crude AL_{ls} and all the filtrates were similar except for the presence of C=O stretching at 1712 cm^{-1} in all the filtrates, associated with conjugated ketone, carbonyl or carboxyl groups (Fig. 5b), suggesting the hydrolysis of the γ-lactone rings or ester intermolecular linkages by HCl to carbonyl and carboxyl groups. Although all the filtrates exhibited unaltered chemical structures from progressive water washing, lowering Na contents from filtrate 2 to filtrate 4 suggests sodium to be weakly bound with AL_{ls}, perhaps by chelating with the oxygen donor ligands as previously observed between sodium ions and polyphenols.[39] The chelated structure is unstable and easily disrupted by progressive water rinsing.

The filtrates were less thermally stable than crude AL_{ls}, attributed to the structural changes in AL_{ls} from HCl washing as indicated by the FTIR spectrum (Fig. 5c and d). The filtrates also exhibited much higher mass loss rates (V) above 500 °C, *i.e.*, mass loss per degree increase in temperature, than crude AL_{ls}, *i.e.*, $V_{\text{filtrate 4}} > V_{\text{filtrate 3}} > V_{\text{filtrate 2}} > V_{\text{crude ALls}}$. Correspondingly, the mass losses at 600 °C increased from 40 wt% in crude AL_{ls}, to 60,

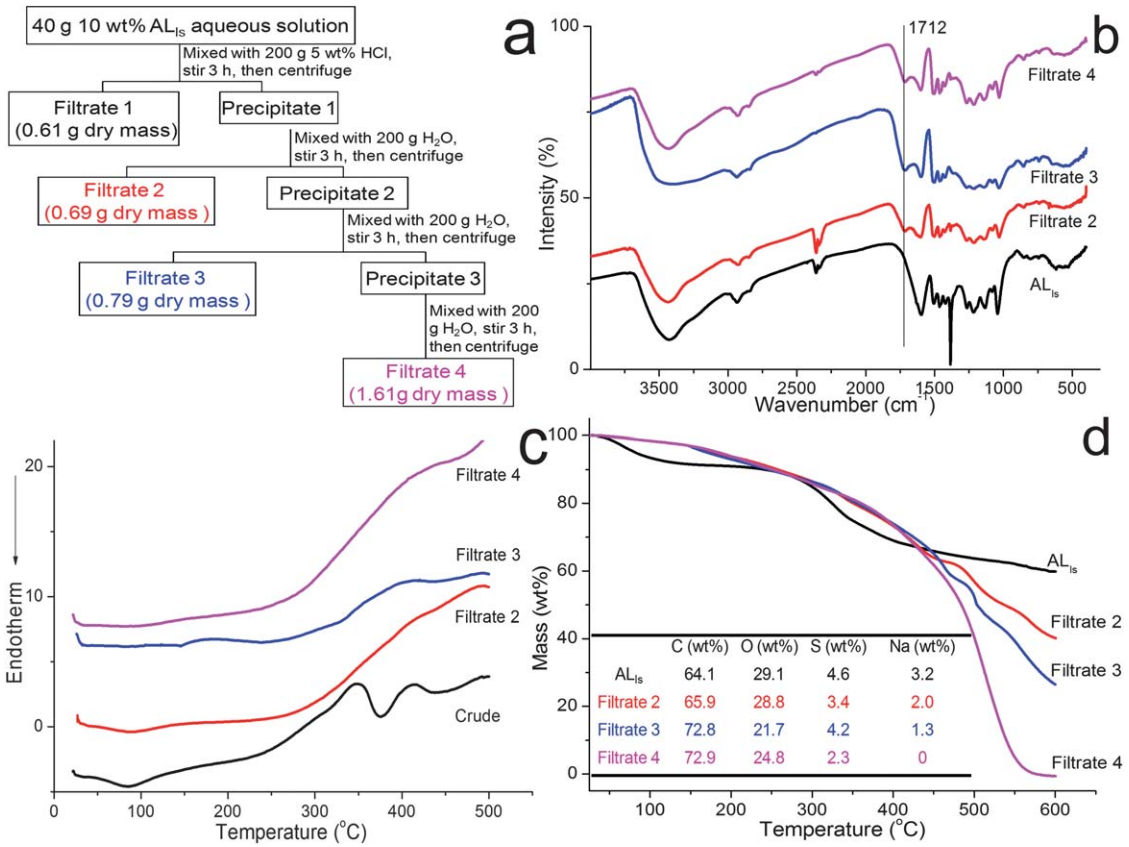

Fig. 5 HCl and water rinsing of AL$_{ls}$: (a) procedures and mass balance; (b) FTIR; (c) DSC; (d) TGA and elemental contents by EDS.

73 and 100 wt% in filtrates 2, 3 and 4, respectively. These increasing mass losses above 500 °C suggest that the heat-induced reactions of crude AL$_{ls}$, such as condensation and crosslinking, which could prevent the structural breakdown to volatiles and/or combustibles, and hence mass loss, may be hindered in the filtrates. The decreasing mass retention above 500 °C is also consistent with the decreasing Na contents from crude AL$_{ls}$ to filtrate 4. Since the filtrates are structurally similar to AL$_{ls}$ as indicated by FTIR, the lowered thermal properties observed are attributed to their lowered sodium contents, affirming the important role of sodium in the thermal transformation of AL$_{ls}$ above 500 °C, including charring and carbonization.

3.5 Porous structures and specific surfaces of CFs and ACFs

Crude AL$_{ls}$ powder and CFs exhibited type II BET nitrogen adsorption–desorption isotherms, typical of non-porous and macroporous materials with weak affinities to nitrogen (Fig. 6a). While crude AL$_{ls}$ powder showed a few pores over the entire micro to macro pore size range, both CFs were mostly macroporous as shown by the pore width distribution curves (Fig. 6b). CFs carbonized at 850 °C had a BET surface area of 13 m^2 g^{-1}, nearly twice that of the 7 m^2 g^{-1} for those carbonized at 600 °C, while their BJH mesopore surface areas and pore volumes were similar, around 2 m^2 g^{-1} and 0.015 cm^3 g^{-1}, respectively. The higher surface area of CF 850 is thought to be due to the higher amount of micropores generated at the higher carbonization temperature. Nevertheless, the limited BET surface areas in CFs indicate that significant micropores and mesopores could not be obtained by just increasing carbonization temperatures without the aid of activating chemicals.

ACFs activated by NaOH and KOH exhibited type IV nitrogen adsorption–desorption isotherms, characteristic of microporous and mesoporous materials with strong sorbent affinities (Fig. 7a and b). For NaOH activated ACFs, the mesopore surface area and volume increased by more than five times, from 55 m^2 g^{-1} and 0.08 cm^3 g^{-1} to 318 m^2 g^{-1} and 0.43 cm^3 g^{-1}, with increasing impregnation ratios from 0.1 to 0.3, respectively, then remained similar around 324 m^2 g^{-1} and 0.44 cm^3 g^{-1} at a 0.5 impregnation ratio. The micropore surface area and volume also more than doubled from 448 m^2 g^{-1} and 0.21 cm^3 g^{-1}, to 1045 m^2 g^{-1} and 0.48 cm^3 g^{-1}, but then dropped to 650 m^2 g^{-1} and 0.3 cm^3 g^{-1}, respectively, at the same increasing impregnation ratios. Combining all mesopores and micropores, the total BET surface area increased by 2.7 times and pore volume increased by 3 times, from 534 m^2 g^{-1} and 0.3 cm^3 g^{-1}, to 1444 m^2 g^{-1} and 0.91 cm^3 g^{-1}, and then decreased to 1027 m^2 g^{-1} and 0.75 cm^3 g^{-1} at the 0.1, 0.3 and 0.5 impregnation ratios, respectively (Fig. 7c and g). It should be noted that the proportion of the total pore volume occupied by micropores decreased from 70.0% to 52.7%, and then 40.0%, showing transformation from micropore-dominant to mesopore-dominant structures as the NaOH impregnation ratio increased from 0.1 to 0.5.

 This journal is © The Royal Society of Chemistry 2013

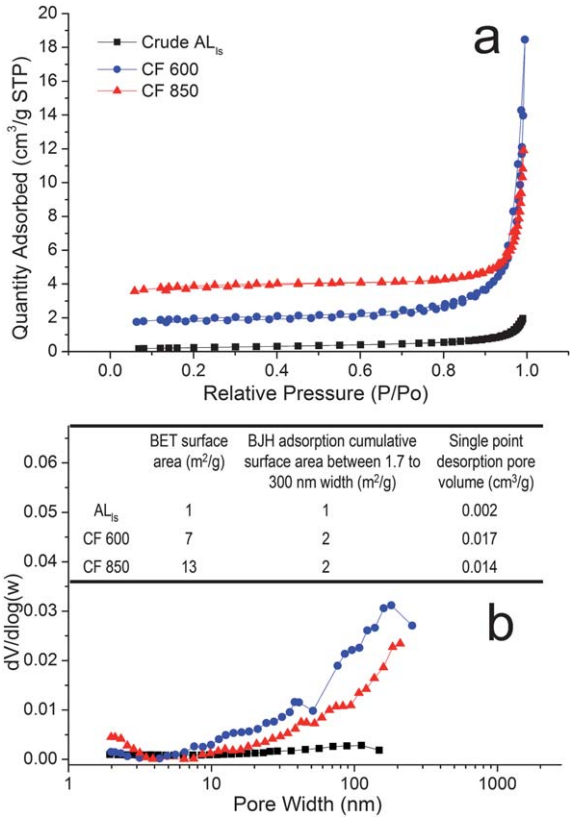

Fig. 6 Nitrogen adsorption–desorption of crude AL_{ls} powder (■) and CF fibers (9/1 AL_{ls}–PEO) carbonized at 600 °C (●, CF-600) and 850 °C (▲, CF-850) (0.5 h, N_2): (a) isotherm; (b) BJH pore distribution.

For KOH activated ACFs, the mesopore surface area and pore volume increased continuously from 44 $m^2\ g^{-1}$ and 0.06 $cm^3\ g^{-1}$, to 63 $m^2\ g^{-1}$ and 0.08 $cm^3\ g^{-1}$, then to 119 $m^2\ g^{-1}$ and 0.19 $cm^3\ g^{-1}$, while the micropore surface area and pore volume also increased in similar magnitudes from 380 $m^2\ g^{-1}$ and 0.18 $cm^3\ g^{-1}$, to 547 $m^2\ g^{-1}$ and 0.25 $cm^3\ g^{-1}$, then to 1197 $m^2\ g^{-1}$ and 0.55 $cm^3\ g^{-1}$, leading to the increasing total BET surface areas and total pore volumes from 446 $m^2\ g^{-1}$ and 0.24 $cm^3\ g^{-1}$, to 634 $m^2\ g^{-1}$ and 0.34 $cm^3\ g^{-1}$, then to 1407 $m^2\ g^{-1}$ and 0.77 $cm^3\ g^{-1}$, with increasing impregnation ratios of 0.1, 0.3 and 0.5, respectively (Fig. 7d). The proportions of micropore volume remained majority and showed only a very slight decrease from 75.0% to 73.5%, and then to 71.4%. These observations clearly showed the micropore-dominant nature of all three KOH activated ACFs.

For NaOH activated ACFs, the adsorption–desorption isotherm transitioned from H4 hysteresis at a 0.1 ratio to H2 hysteresis at the 0.3 and 0.5 ratios. H4 type hysteresis consists of parallel adsorption and desorption branches and has been associated with micropore characteristics.[40,41] As suggested by the BJH mesopore and *t*-plot derived micropore distribution, a few mesopores and widely distributed micropores in the 0.7–1.9 nm range were observed at the 0.1 impregnation ratio, also confirming its micropore-dominant structure. The enclosure of the desorption branch at a relative pressure P/P_o of 0.1 indicated that those micropores were most likely slit-like. For both ACFs activated at the 0.3 and 0.5 ratios, the H2 type hysteresis with a steeper adsorption than desorption branch is more typical of mesoporous materials with rather broad pore size and shape distributions, possibly including narrow necks and wide bodied interconnected pore-network structures where pore blocking and percolation may occur.[40,41] The interconnecting porous structure associated with H2 hysteresis has been described by the ink-bottle model, where the larger mesopore bodies were connected through much smaller mesopores and/or micropore necks.[42,43] At the 0.3 and 0.5 impregnation ratios, the step-down in the desorption isotherm around 0.45 P/P_o indicates evaporation during desorption to involve the cavitation mechanism, where the neck size is smaller than the 5 nm critical size for N_2 at 77 K.[43] The BJH pore size distribution derived from the adsorption branch showed that the mesopores were distributed between 5 and 25 nm with peaks around 8 and 10 nm at the 0.3 and 0.5 ratios, respectively (Fig. 7c), while the BJH neck size distribution derived from the desorption branch exhibited distinct peaks at 4 nm at both 0.3 and 0.5 ratios. Although this peak was reported to be the artificial spike determined by the thermal physical state of the N_2 fluid during evaporation rather than the actual neck sizes,[44] its presence is consistent with the cavitation mechanism during desorption, hence the less than 5 nm neck size ink-bottle structure within ACFs (Fig. 7e). The micropores were between 0.7 and 1.5 nm at both 0.3 and 0.5 ratios (Fig. 7g), which are in agreement with previously reported micropore size distribution of NaOH activated carbon particulates.[45]

Similarly, the step-down in the desorption isotherm also occurred around 0.45 P/P_o at the 0.3 and 0.5 KOH/AL_{ls} impregnation ratios, indicating that the micropores are not isolated slit-like but act as the inter-connecting matrix for the mesopores.[46] The corresponding pore width distributions showed very limited mesopores at the 0.1 and 0.3 impregnation ratios, while a mesopore peak appeared at 30 nm at the 0.5 ratio (Fig. 7d). The characteristic peaks at around 4 nm derived from the desorption branches of the isotherm were also observed at both 0.3 and 0.5 ratios (Fig. 7f), again confirming the micro/mesopore arrays to be possibly ink-bottle structures with neck sizes smaller than 5 nm. The micropore sizes ranged from 0.7 to 1.9 nm and peaked around 0.75 nm, becoming more prominent as the ratios increased from 0.1 to 0.5 (Fig. 7h). This suggests potassium atom clusters to be of that particular size which is consistent with the pore size of other KOH activated carbon materials.[47,48]

The pore structures of ACFs activated by NaOH and KOH exhibited some similarities as well as obvious differences at the same impregnation ratios. For instance, at the highest impregnation ratio of 0.5, both ACFs had type IV nitrogen adsorption isotherms, showing their dual microporous and mesoporous nature, as well as similar total pore volumes. Both ACFs had rough surfaces shown by AFMs (Fig. 8a and b), indicative of surface porosity. The similar surface roughness observed could result from the simultaneous activation process where the reduction of alkali metal hydroxides and the violent motions of these metal atoms and atom clusters intercalated between layers of polyaromatic/nonaromatic hydrocarbons in the bulk as well as near the fiber surfaces, cause rough and

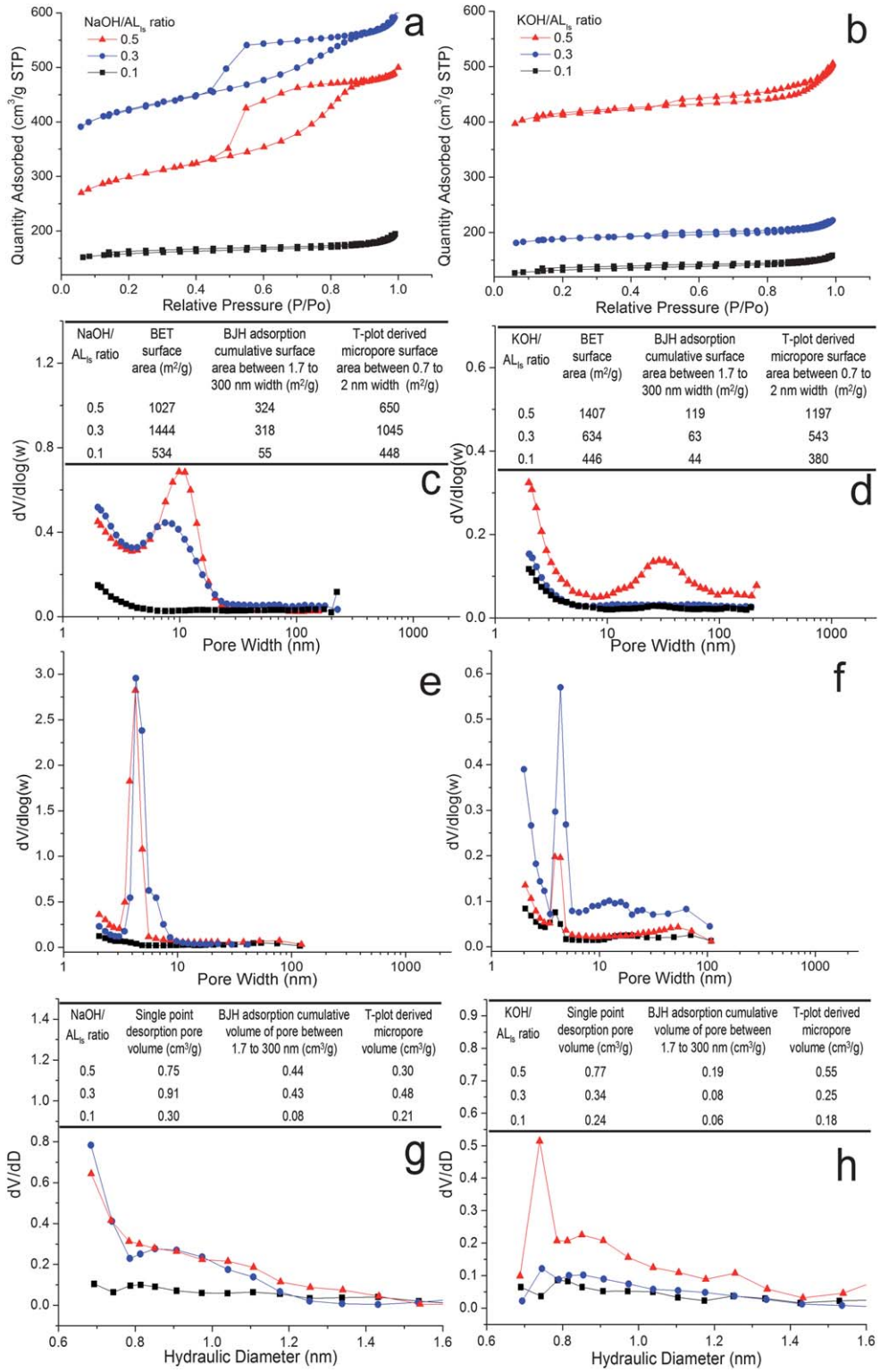

NaOH/ AL$_{ls}$ ratio	BET surface area (m^2/g)	BJH adsorption cumulative surface area between 1.7 to 300 nm width (m^2/g)	T-plot derived micropore surface area between 0.7 to 2 nm width (m^2/g)
0.5	1027	324	650
0.3	1444	318	1045
0.1	534	55	448

KOH/ AL$_{ls}$ ratio	BET surface area (m^2/g)	BJH adsorption cumulative surface area between 1.7 to 300 nm width (m^2/g)	T-plot derived micropore surface area between 0.7 to 2 nm width (m^2/g)
0.5	1407	119	1197
0.3	634	63	543
0.1	446	44	380

NaOH/ AL$_{ls}$ ratio	Single point desorption pore volume (cm^3/g)	BJH adsorption cumulative volume of pore between 1.7 to 300 nm (cm^3/g)	T-plot derived micropore volume (cm^3/g)
0.5	0.75	0.44	0.30
0.3	0.91	0.43	0.48
0.1	0.30	0.08	0.21

KOH/ AL$_{ls}$ ratio	Single point desorption pore volume (cm^3/g)	BJH adsorption cumulative volume of pore between 1.7 to 300 nm (cm^3/g)	T-plot derived micropore volume (cm^3/g)
0.5	0.77	0.19	0.55
0.3	0.34	0.08	0.25
0.1	0.24	0.06	0.18

Fig. 7 Nitrogen adsorption–desorption of ACFs from 9/1 AL$_{ls}$–PEO electrospun and activated with NaOH (a and c, *e.g.*) and KOH (b, d, f, and h) at different alkali hydroxide/AL$_{ls}$ ratios and carbonized (850 °C, 0.5 h, N_2): (a and b) isotherm; (c and d) BJH pore/cavity width distribution; (e and f) BJH neck size distribution; (g and h) micropore hydraulic diameter distribution. Inset tables: (c and d) BET surface area, BJH adsorption cumulative surface area and *t*-plot micropore surface area; (g and h) single point desorption pore volume, BJH adsorption cumulative pore volume and *t*-plot derived micropore volume.

uneven surfaces. The desorption branch of the isotherms in both NaOH and KOH activated ACFs showed step-down at 0.45 P/P_o, suggesting that the micro/mesopore arrays were interconnected possibly *via* ink-bottle structures with neck size less than 5 nm. However, ACFs activated with NaOH showed a clearly different H2 hysteresis than the H4 hysteresis from KOH

 This journal is © The Royal Society of Chemistry 2013

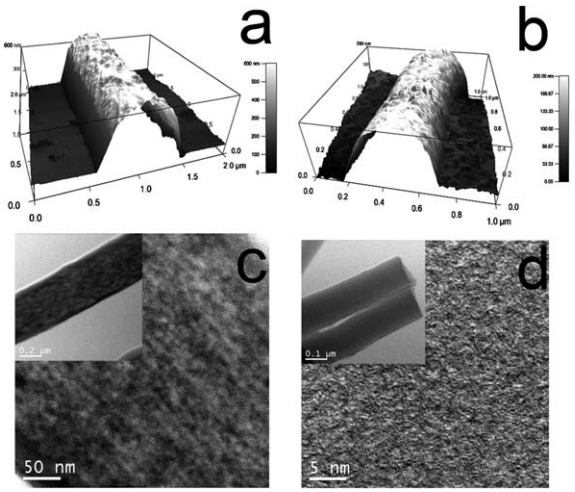

Fig. 8 Morphology of ACFs from electrospun 9/1 AL_{ls}–PEO hybrid fibers activated with NaOH (a and c) and KOH (b and d) at 0.5 alkali hydroxide/AL_{ls} ratios and carbonized (850 °C, 0.5 h, N_2): AFM 3D imaging (a and b); TEM (c and d).

activation, indicating that the NaOH activated ACFs had much higher mesopore volume (58.7% *vs.* 24.8%), but less micropores than those activated by KOH (40.0% *vs.* 71.4%) (Fig. 7c and d). As shown in the TEMs, NaOH conferred a much less dense structure than KOH on ACFs. With NaOH, pores were observed within the bulk of the fibers and seemed to be enclosed by cylindrical domains that were a few hundred nm long and parallel to the fiber axis (Fig. 8c), while pores activated by KOH could not be discerned within the bulk of the fibers (Fig. 8d). Meanwhile, NaOH activated ACFs exhibited clearly visible surface mesopores larger than 5 nm (Fig. 8c), while those activated with KOH exhibited mainly micropores less than 2 nm (Fig. 8d). The *t*-plot and the BJH cumulative pore with distribution more reflective of the bulk pore size showed that ACFs from NaOH activation had broad micropores from 0.7 to 1.5 nm and mesopores between 5 and 25 nm peaking at 10 nm, while ACFs from KOH activation had micropores mainly around 0.75 nm and mesopores from 10 to 50 nm peaking at 30 nm. The different porous structures formed appeared to be closely associated with the sizes of the Na and K atoms and their atomic clusters and how they behave during the activation process.

In summary, both NaOH and KOH activated ACFs contained both mesopores and micropores but in different sizes and proportions. The pores within the ACFs tended to be isolated slit-like micropores at a 0.1 impregnation ratio, but developed into a network of larger mesopores connected or embedded within the micropore matrix by narrow necks as the ratios increased to 0.3 and 0.5, along with the increase in the proportion of mesopores. The maximum BET surface area exceeding 1400 $m^2\ g^{-1}$ and pore volumes from 0.77 to 0.91 $cm^3\ g^{-1}$, were reached at the 0.3 and 0.5 impregnation ratios for ACFs activated by NaOH and KOH, respectively. Those values were comparable to PACs activated by the same but considerably lower alkali hydroxides,[11] *i.e.*, at only one-fifth of activating alkaline hydroxide quantities. The attainment of similar pore quality with far less alkali hydroxides may be attributed to their close association with the AL_{ls} carbon precursor in the aqueous mixtures, clearly evident from the superior pore production efficiency of this approach. This *in situ* incorporation of activating alkali hydroxides in the aqueous spin dopes and single-step simultaneous carbonization/activation process have demonstrated to be effective in producing superiorly porous ACFs while being chemically and energetically economical and advantageous over conventional approaches.

4 Conclusion

Sub-micrometer sized (100–500 nm) ACFs have been robustly fabricated by single-step carbonization/activation of hybrid precursor fibers electrospun from predominantly AL_{ls} aqueous mixtures with impressively low activating alkali hydroxides, typically less than 50% of the AL_{ls} carbon precursor. The incorporation of the PEO carrier was effective in facilitating the necessary chain entanglement to generate fibers by electrospinning as well as providing thermal stabilization while not interfering with the thermal decomposition and structural transformation of AL_{ls} to carbon by heating to 850 °C under N_2. Activation with either NaOH or KOH was effective at significantly lower impregnation ratios ($\leq$0.5), *i.e.*, one tenth to one quarter of the current industrial standard, to transform non-porous AL_{ls}–PEO hybrid precursor fibers into highly porous ACFs with specific surfaces and pore volumes of up to 1400 $m^2\ g^{-1}$ and 0.91 $cm^3\ g^{-1}$, respectively. ACFs activated by NaOH contained both mesoporosity and microporosity, attaining a maximum specific surface of 1440 $m^2\ g^{-1}$ and a pore volume of 0.91 $cm^3\ g^{-1}$ at a 0.3 impregnation ratio. The KOH activated ACFs, on the other hand, showed mainly microporosity where both surface area and pore volume increased with increasing impregnation ratios from 0.1 to 0.5, reaching 1407 $m^2\ g^{-1}$ and 0.77 $cm^3\ g^{-1}$, respectively. This approach of incorporating a multi-functional PEO carrier and the *in situ* impregnation of NaOH and KOH with AL_{ls} has shown to be highly effective in facilitating robust fiber formation and simultaneous carbonization and activation, producing very high specific surface ACFs with mesopores and micropores at impressively low alkali hydroxides–AL_{ls} impregnation ratios. Overall, this approach of achieving superiorly porous and high specific surface ACFs from the abundant lignin carbon precursor with minimal chemical and thermal input presents multiple advantages and is potentially applicable to other polyphenolics.

Notes and references

1 I. A. Pearl, *The Chemistry of Lignin*, Dekker, 1967, pp. 106–127.
2 J. F. Kadla, S. Kubo, R. A. Venditti, R. D. Gilbert, A. L. Compere and W. Griffith, *Carbon*, 2002, **40**, 2913–2920.
3 S. Kubo and J. F. Kadla, *J. Polym. Environ.*, 2005, **13**, 97–105.
4 J. L. Braun, K. M. Holtman and J. F. Kadla, *Carbon*, 2005, **43**, 385–394.
5 K. Sudo and K. Shimizu, *J. Appl. Polym. Sci.*, 1992, **44**, 127–134.
6 Y. Uraki, R. Taniwatashi, S. Kubo and Y. Sano, *J. Wood Sci.*, 2000, **46**, 52–58.

7 J. Hayashi, A. Kazehaya, K. Muroyama and A. P. Watkinson, *Carbon*, 2000, **38**, 1873–1878.
8 L. Khezami, A. Chetouani, B. Taouk and R. Capart, *Powder Technol.*, 2005, **157**, 48–56.
9 K. Babel and K. Jurewicz, *Carbon*, 2008, **46**, 1948–1956.
10 S. I. Mussatto, M. Fernandes, G. J. M. Rocha, J. J. M. Orfao, J. A. Teixeira and I. C. Roberto, *Bioresour. Technol.*, 2010, **101**, 2450–2457.
11 V. Fierro, V. Torne-Fernandez and A. Celzard, *Microporous Mesoporous Mater.*, 2007, **101**, 419–431.
12 H. Marsh and F. Rodriguez-Reinoso, *Activated carbon/Harry Marsh, Francisco Rodriguez-Reinoso*, Elsevier, 2006.
13 A. Ahmadpour and D. D. Do, *Carbon*, 1996, **34**, 471–479.
14 T. Otowa, Y. Nojima and T. Miyazaki, *Carbon*, 1997, **35**, 1315–1319.
15 M. J. B. Evans, E. Halliop and J. A. F. McDonald, *Carbon*, 1999, **37**, 269–274.
16 Y. Sudaryanto, S. B. Hartono, W. Irawaty, H. Hindarso and S. Ismadji, *Bioresour. Technol.*, 2006, **97**, 734–739.
17 M. A. Daley, C. L. Mangun, J. A. DeBarr, S. Riha, A. A. Lizzio, G. L. Donnals and J. Economy, *Carbon*, 1997, **35**, 411–417.
18 I. Mochida, S. Kawano, M. Hironaka, S. Yatsunami, Y. Korai, Y. Matsumura and M. Yoshikawa, *Chem. Lett.*, 1995, 385–386.
19 M. Lordgooei, K. R. Carmichael, T. W. Kelly, M. J. Rood and S. M. Larson, *Gas Sep. Purif.*, 1996, **10**, 123–130.
20 S. Y. Jiang, J. A. Zollweg and K. E. Gubbins, *J. Phys. Chem.*, 1994, **98**, 5709–5713.
21 S. H. Lin and F. M. Hsu, *Ind. Eng. Chem. Res.*, 1995, **34**, 2110–2116.
22 C. Brasquet and P. LeCloirec, *Carbon*, 1997, **35**, 1307–1313.
23 I. Tanahashi, A. Yoshida and A. Nishino, *Carbon*, 1990, **28**, 477–482.
24 I. Tanahashi, A. Yoshida and A. Nishino, *Carbon*, 1991, **29**, 1033–1037.
25 S. H. Byeon, S. M. Oh, W. S. Kim and C. H. Lee, *Ind. Health*, 1997, **35**, 404–414.
26 Y. Uraki, A. Nakatani, S. Kubo and Y. Sano, *J. Wood Sci.*, 2001, **47**, 465–469.
27 R. Ruiz-Rosas, J. Bedia, M. Lallave, I. G. Loscertales, A. Barrero, J. Rodriguez-Mirasol and T. Cordero, *Carbon*, 2010, **48**, 696–705.
28 H. Q. Liu and Y. L. Hsieh, *J. Polym. Sci., Part B: Polym. Phys.*, 2003, **41**, 953–964.
29 P. Lu and Y. L. Hsieh, *J. Membr. Sci.*, 2009, **330**, 288–296.
30 R. S. Mikhail, S. Brunauer and E. E. Bodor, *J. Colloid Interface Sci.*, 1968, **26**, 45–53.
31 W. D. Harkins and G. Jura, *J. Chem. Phys.*, 1943, **11**, 431–432.
32 S. Moldoveanu, in *Techniques and instrumentation in analytical chemistry*, Elsevier, 1998, vol. 20, pp. 327–350.
33 E. Dorrestijn, L. J. J. Laarhoven, I. W. C. E. Arends and P. Mulder, *J. Anal. Appl. Pyrolysis*, 2000, **54**, 153–192.
34 M. A. Scheijen, J. J. Boon, W. Hass and V. Heemann, *J. Anal. Appl. Pyrolysis*, 1989, **15**, 97–120.
35 W. M. G. M. Vanloon, J. J. Boon and B. Degroot, *Environ. Sci. Technol.*, 1993, **27**, 2387–2396.
36 R. K. Sharma, J. B. Wooten, V. L. Baliga, X. H. Lin, W. G. Chan and M. R. Hajaligol, *Fuel*, 2004, **83**, 1469–1482.
37 S. Kubo, Y. Uraki and Y. Sano, *Carbon*, 1998, **36**, 1119–1124.
38 M. Kleen and G. Gellerstedt, *J. Anal. Appl. Pyrolysis*, 1995, **35**, 15–41.
39 C. B. Black, H. W. Huang and J. A. Cowan, *Coord. Chem. Rev.*, 1994, **135**, 165–202.
40 K. S. W. Sing, D. H. Everett, R. A. W. Haul, L. Moscou, R. A. Pierotti, J. Rouquerol and T. Siemieniewska, *Pure Appl. Chem.*, 1985, **57**, 603–619.
41 S. Kaskel, *Characterisation of porous solids VIII: proceedings of the 8th International Symposium on the Characterisation of Porous Solids*, ed. S. Kaskel, *et al.*, RSC Publishing, 2009.
42 M. Thommes, B. Smarsly, M. Groenewolt, P. I. Ravikovitch and A. V. Neimark, *Langmuir*, 2006, **22**, 756–764.
43 P. I. Ravikovitch and A. V. Neimark, *Langmuir*, 2002, **18**, 9830–9837.
44 J. C. Groen, L. A. A. Peffer and J. Perez-Ramirez, *Microporous Mesoporous Mater.*, 2003, **60**, 1–17.
45 P. J. M. Carrott, M. M. L. R. Carrott and P. A. M. Mourao, *J. Anal. Appl. Pyrolysis*, 2006, **75**, 120–127.
46 Q. Z. Guozhong Cao and C. Jeffery Brinker, in *Annual review of nanoresearch*, World Scientific, 2006, pp. 540–542.
47 A. Ahmadpour and D. D. Do, *Carbon*, 1997, **35**, 1723–1732.
48 E. Raymundo-Pinero, K. Kierzek, J. Machnikowski and F. Beguin, *Carbon*, 2006, **44**, 2498–2507.

 This journal is © The Royal Society of Chemistry 2013